NADPH oxidase-derived H2O2 subverts pathogen signaling by oxidative phosphotyrosine conversion to PB-DOPA

Biological Sciences – Microbiology

NADPH oxidase-derived H_2O_2 subverts pathogen signaling by oxidative phosphotyrosine conversion to PB-DOPA

Short title: Oxidative p-Tyr to DOPA conversion in host defense

Luis AJ Alvarez[1], Lidija Kovačič[2#], Javier Rodríguez[3$], Jan-Hendrik Gosemann[1], Malgorzata Kubica[2], Gratiela Pircalabioru[2], Florian Friedmacher[1], Ada Cean[4], Alina Ghişe[4], Mihai B Sărăndan[4], Prem Puri[1], Simon Daff[5], Erika Plettner[6], Alexander von Kriegsheim[3$], Billy Bourke[1,2,7*], Ulla G Knaus[1,2,7*]

[1]National Children's Research Center, Our Lady's Children's Hospital Crumlin, Dublin, Ireland; [2]Conway Institute, School of Medicine and [3]Systems Biology Ireland, University College Dublin, Dublin, Ireland; [4]Faculty of Veterinary Medicine, Banat University of Agricultural Sciences and Veterinary Medicine "King Michael I of Romania", Timisoara, Romania; [5] School of Chemistry, University of Edinburgh, Edinburgh, United Kingdom; [6]Department of Chemistry, Simon Fraser University, Burnaby, Canada.

[7]Co-senior author # Current address: Novartis Ireland Ltd, Dublin, Ireland

$ Current address: University of Edinburgh, Edinburgh, United Kingdom

[*] Correspondence to

Ulla Knaus, Conway Institute, University College Dublin, Belfield, Dublin 4, Ireland; Tel: +353-1-7166719; Ulla.Knaus@ucd.ie

Billy Bourke, National Childrens' Research Center, Our Lady's Childrens Hospital Crumlin, Dublin 12, Ireland; Billy.Bourke@ucd.ie

Key words: NADPH oxidase, bacterial tyrosine phosphorylation, DOPA, mucosal immunity

Abstract

Strengthening the host immune system to fully exploit its potential as antimicrobial defense is vital in countering antibiotic resistance. Chemical compounds released during bidirectional host-pathogen crosstalk that follows a sensing-response paradigm, can serve as protective mediators. A potent, diffusible messenger is hydrogen peroxide (H_2O_2), but its consequences on extracellular pathogens are unknown. Here we show that H_2O_2, released by the host on pathogen contact, subverts the tyrosine signaling network of a number of bacteria accustomed to low-oxygen environments. This defense mechanism utilizes heme-containing bacterial enzymes with peroxidase-like activity to facilitate phosphotyrosine (p-Tyr) oxidation. An intrabacterial reaction converts p-Tyr to protein-bound 3,4-dihydroxyphenylalanine (PB-DOPA) via a tyrosinyl radical intermediate, thereby altering antioxidant defense and inactivating enzymes involved in polysaccharide biosynthesis and metabolism. Disruption of bacterial signaling by DOPA modification reveals an infection containment strategy that weakens bacterial fitness and could be a blueprint for antivirulence approaches.

Significance Statement

Mucosal barrier tissues participate in immune defense in infections, but NADPH oxidases expressed in these epithelia are much less efficient in their oxidant output than the phagocyte oxidase. The importance of releasing low H_2O_2 concentrations as host defense mechanism against pathogens remains unclear. Here, we demonstrate that nano to submicromolar H_2O_2 disrupts the tyrosine phosphorylation network in several pathogens by an oxidative dephosphorylation process. This is accomplished by irreversible chemical modification of key phosphotyrosine residues, which in turn changes protein activity without affecting bacterial viability. This process is a host-initiated antivirulence strategy, reducing the fitness of pathogens in the extracellular space.

\body

Introduction

Communication between the host and pathogens at the mucosal interface is governed by the chemical environment. Host-derived signals can be subverted by pathogens to enhance virulence gene expression and pathogen expansion (1), but in most circumstances the immune system prevails by coordinating defense mechanisms, thereby restricting colonization and disease. Within complex mucosal environments pathogen virulence can be modulated in a niche-specific manner (2), which is now recognized as an important strategy that helps combating antibacterial resistance. The most promising approach to target bacterial virulence factors are compounds that affect multiple prokaryotic targets at once.

As a relatively stable, diffusible mediator host-derived hydrogen peroxide (H_2O_2) can modify more distant targets. H_2O_2 can penetrate bacterial membranes inducing transcriptional stress responses (3), but may also alter other cellular processes via oxidation. High concentrations of reactive oxygen species (ROS) and derivatives (HOCl) can induce irreversible amino acid oxidations or chlorinations, leading to loss of function by misfolding or degradation and to bacterial killing. Lower ROS levels, in particular H_2O_2, primarily result in oxidative modifications that are dynamic and reversible, such as thiol oxidation and disulfide bond formation in enzymes, iron-sulfur clusters or transcriptional regulators containing redox-sensitive cysteine residues. The redox sensitivity of mammalian tyrosine kinase pathways is mainly due to transient inactivation of protein tyrosine phosphatases or by oxidative protein kinase activation (e.g. SRC, ASK1) (4). Intestinal pathogens traversing through the mucus before attaching to and/or invading the epithelium can activate epithelial NADPH oxidases (NOX1, DUOX2) before recruitment of neutrophils occurs. Neutrophils engulfing bacteria produce and release large

quantities of $O_2^{\bullet-}$ via NOX2 into the phagosome, which enables bacterial killing by the concerted action of HOCl, proteases and antibacterial peptides (5). Intestinal epithelial cells (IEC) release low levels of H_2O_2 into the lumen, but the achievable concentrations are in the nano/micromolar range and inadequate for bactericidal activity. We hypothesized that, when maintained over time, IEC-derived H_2O_2 may overcome antioxidant defenses of pathogens and may alter redox-regulated processes in bacteria.

Bearing in mind how H_2O_2 acts on mammalian signaling circuits, the prime target for redox regulation in prokaryotes are tyrosine kinase pathways. Tyrosine phosphorylation coordinates a variety of key processes in bacteria including biofilm and capsule formation, heat shock response, DNA replication, transcription, metabolic processes, antibiotic resistance, virulence and interspecies communication (6). Bacterial tyrosine (BY) kinases contain ATP-binding Walker motifs and a C-terminal tyrosine cluster, and exhibit no sequence or structural homology to eukaryotic kinases (7). These BY-kinases cooperate with phosphatases, various association partners and Hanks type serine/threonine kinases in interaction networks, but mechanistic details of their regulation and often even the identity of the kinase(s) remains poorly understood. Nevertheless, interfering with BY-kinase signaling should be beneficial as decreased virulence has been connected to interference with BY-kinase pathways (8, 9). Here we show that H_2O_2-mediated disruption of the bacterial tyrosine signaling is a common feature in intestinal and even pulmonary pathogens, requiring low H_2O_2 concentrations in physiological conditions and a combination of host and bacterial features present in oxygen-restricted environments during infections. In contrast to increased phosphotyrosine (p-Tyr) signaling by phosphatase inhibition via thiol oxidation in mammalian systems, H_2O_2 triggered iron-associated conversion of p-Tyr to 3', 4'-dihydroxyphenylalanine (DOPA) on bacterial proteins, leading to

disruption of p-Tyr signaling. Proteomics data reveal that this interference with p-Tyr signaling occurs frequently in prokaryotic and eukaryotic organisms.

Results

H_2O_2 disrupts phosphotyrosine signaling of pathogens

The pathogens *L. monocytogenes*, *S. enterica* serovar Typhimurium and *K. pneumoniae* were chosen as representative enteric bacteria with diverse cell wall structures, motility and antioxidant defense gene expression to determine if host epithelial H_2O_2 production accompanies intestinal infection as a general defense mechanism. All of these bacteria induced H_2O_2 release when incubated with IECs (HCT-8 cells, Fig. 1a), an effect suppressed by the cell-permeable pan-oxidase inhibitor DPI and catalase. Previously, we connected H_2O_2 generation upon pathogen contact in this cell type directly to NOX1, the only NADPH oxidase expressed (8). Bacterial infection triggered translocation of the NOX-$p22^{phox}$ complex to the plasma membrane (Fig. S1a; visualized as $p22^{phox}$), inducing continuous release of low H_2O_2 concentrations (20nmol H_2O_2/h/mg protein). A similar H_2O_2 concentration is achieved on top of a Boyden chamber filter with Cos cells expressing constitutively active NOX4 seeded on the bottom (15nmol H_2O_2/h/mg protein, Fig. 1a). In human colon biopsies, a physiologically relevant model expressing NOX1, *L. monocytogenes* infection caused upregulation and membrane recruitment of the NOX-$p22^{phox}$ complex concurrently with H_2O_2 generation (Fig. 1b, Fig. S1b). ROS generation was also detected *in vivo* using a ligated rabbit ileal loop infection model. Injection of *L. monocytogenes* or *Campylobacter jejuni* led to severe tissue injury in rabbits, preceded by recruitment of the NOX dimerization partner $p22^{phox}$ to the apical crypt surface and oxidative modification of epithelia by carbonylation (Fig. 1c, Fig. S1c-e). These data indicate that gut epithelial H_2O_2 generation by NADPH oxidase is commonly observed in infection.

The majority of bacteria remain extracellular in the mucus layer or gut lumen at any particular time point of infection, either because only a certain fraction will invade epithelial

cells (e.g. *Listeria*) or because particular pathogens attach to but do not invade IECs (e.g. *Klebsiella*). Released H_2O_2 is taken up by bacteria and induces a transcriptional stress response, but we speculated that H_2O_2 may also alter tyrosine kinase pathways. Immunoblot analysis of extracellular bacteria recovered from media of infected IECs, from the top of the filter of Cos-NOX4 cells or from biopsy media revealed not increased, but significantly decreased bacterial p-Tyr content when H_2O_2 was present (Fig. 1d-f). Bacterial viability or overall bacterial protein content were not altered (Fig. S1f-i; Fig S2b).Tyrosine phosphorylation of Wzc, the main BY-kinase expressed in *K. pneumoniae*, *E. coli* and *Acinetobacter* (7), was substantially lower, while Wzc expression was not altered (Fig. S2a). These observations were further confirmed by analyzing bacteria recovered from the rabbit ileal lumen after infection. Overall tyrosine phosphorylation was significantly diminished in extracellular bacteria, while protein content was comparable to the starting bacterial culture (Fig. 1g, Fig.S1j).

Imlay and coworkers reported that a bacterial culture in iron-rich media decomposed 0.5mM H_2O_2 in less than 2h without affecting bacterial growth substantially (10), and an intracellular H_2O_2 sensor indicated an up to 500-fold gradient between outside and inside H_2O_2 concentrations in *E. coli* (11). In line with these observations addition of 0.7mM H_2O_2 to bacterial cultures mimicked tissue-based observations without reducing bacterial viability (Fig. S2b), whereas heat treatment did not alter the p-Tyr profile (Fig. S2c, d). Bacterial tyrosine phosphorylation has been connected to pathogenicity (8, 9) and to type 3 secretion system regulation in EHEC (12). If a similar link exists between p-Tyr signaling and *L. monocytogenes* virulence, it should be disrupted by H_2O_2. In accord, adhesion to IECs, which is a prerequisite for *Listeria* invasion, decreased significantly after pre-exposure of *L. monocytogenes* to H_2O_2, resulting in lower internalization of the bacterium (Fig. S2e). Oxidative tyrosine

dephosphorylation may occur also at other mucosal surfaces, in particular in the lung where ROS generated by alveolar macrophages and lung epithelial cells provide host defense. We established a fetal rat lung model that permitted intra-organ incubation with bacteria and subsequent recovery of bacteria and bronchoalveolar fluid (BAF). Intratracheal injection of *S. pneumoniae* caused 2-3-fold increased H_2O_2 levels above the DPI baseline with concomitant decrease of the p-Tyr content in bacteria recovered from the BAF pellet (Fig. S3a, b). The developmental regulation of DUOX expression and the short period of pathogen exposure favored macrophages as H_2O_2 source in this model. Co-culture of *S. pneumoniae* with rat alveolar macrophages prompted increased cell adhesion and protrusions that were accompanied by Nox2 NADPH oxidase upregulation, translocation of Nox2 to the plasma membrane and $O_2^{\bullet-}$ /H_2O_2 production, which was inhibited by DPI (Fig. S3c, d). *S. pneumoniae* itself was not affected by DPI and did not generate H_2O_2 in the low oxygen conditions used throughout (Fig. S3e). Decreased p-Tyr content was detected in extracellular *S. pneumoniae* collected from macrophage co-culture media, similar to our observations in infected rat lungs (Fig. S3f). Adding H_2O_2 as single bolus to growth medium induced *S. pneumoniae* tyrosine dephosphorylation without altering bacterial viability (Fig. S3g). Polysaccharide biosynthesis is to date the only well characterized process regulated by bacterial tyrosine phosphorylation. Pre-exposure of *S. pneumoniae* to H_2O_2 diminished biofilm formation (Fig. S3h-i), thus strengthening the connection between H_2O_2, tyrosine dephosphorylation and pathogenic traits. These results indicate that host H_2O_2 production is coupled to diminished p-Tyr content in extracellular pathogens, leading to decreased pathogenicity by disrupting intrabacterial signaling.

The chemical microenvironment and hemoproteins affect oxidative tyrosine dephosphorylation in bacteria

The change in bacterial p-Tyr content by oxidation suggested a distinct mechanism for phosphate group removal, as thiol-based inactivation of phosphatases would cause increased tyrosine phosphorylation. Further, deletion of PTP1B, the only known phosphatase in *C. jejuni*, did not alter p-Tyr-dependent capsule biosynthesis. We explored the environmental conditions required for the suppression of bacterial p-Tyr by H_2O_2. Intestinal pathogens are typically facultative anaerobes, thriving in the low oxygen levels present in the gut (13), but many bacteria tolerate atmospheric oxygen levels. Environmental adaptation prompts usually global transcriptional responses (14), but these external stress signals may also remodel the bacterial signaling conduit. Comparison of bacteria propagated in low oxygen (5% O_2) versus ambient oxygen (21% O_2) before exposure to H_2O_2 indicated a striking difference. *K. pneumoniae* and *L. monocytogenes* grown in 21% O_2 before addition of H_2O_2 retained their original p-Tyr profile, while cultures grown in 5% O_2 lost the p-Tyr signal (Fig. 2a).

We questioned whether changes in iron availability could affect the p-Tyr network, as oxidative stress in bacteria can induce iron regulators (e.g. Fur, Dps) and inactivate iron-sulfur dehydratases (3). Bacterial cultures initially grown in iron-deficient media at 5% O_2 were analyzed after addition of ferrous sulfate and H_2O_2. The p-Tyr content was only diminished by H_2O_2 when extracellular iron was provided (Fig. 2b). In co-culture conditions where iron is supplied by HCT-8 cells and the culture media, the Fe^{2+} versus Fe^{3+} ratio in the total pool of bacterial intracellular iron was dependent on IEC-mediated H_2O_2 generation (Fig. 2c), suggesting that the bacterial intracellular pool of free ferrous iron was oxidized to ferric iron. Carbonylation, a marker for site-specific, metal-catalyzed protein modification by hydroxyl radicals, was

increased in bacteria exposed to HCT-8-generated H_2O_2 (Fig. 2d). This suggests that oxidative tyrosine dephosphorylation in bacteria is taking place in conditions that are present in the intestine during infections.

Cytochrome P450 or peroxidase activity is required for oxidative dephosphorylation

Many pathogens including certain *Pseudomonas*, *Mycobacterium* or *Acinetobacter* strains contain cytochrome P450 monooxygenases that catalyze hydroxylation reactions via molecular oxygen reduction or by using the peroxide-shunt pathway, contributing to virulence and persistence in the host (15). Expression of an outer membrane/periplasmic cytochrome P450 (Cj1411, CjP450) in *C. jejuni* increased after H_2O_2 exposure and deletion of CjP450 decreased capsular polysaccharide production (16), raising the possibility that CjP450 participates in p-Tyr signaling. Deletion of CjP450 or mutation of a cysteine (C.j. *ΔP450*:*P450C399F*) in the heme-iron ligand signature motif of CjP450 that leads to perturbation of the heme pocket and loss of catalytic activity in P450 enzymes, rendered the *C. jejuni* p-Tyr network insensitive to H_2O_2 (Fig. 3a). To verify direct participation of CjP450 in oxidative tyrosine dephosphorylation, both CjP450 and Gne, a UDP-GlcNAc/Glc 4-epimerase phosphorylated on the active site Tyr^{146} were expressed and purified from *E. coli* (Fig. S4a)(16). Dephosphorylation of Gne was dependent on addition of H_2O_2 and CjP450, and not observed in the presence of catalase and sodium dithionite, respectively (Fig. 3b). When H_2O_2 is available, cytochrome P450s can exhibit peroxidase-like activity (15, 17). We asked if other hemoproteins, such as horseradish peroxidase (HRP), could catalyze this reaction in a similar fashion. Replacing CjP450 with HRP during exposure of Gne to H_2O_2 removed p-Tyr equally efficiently (Fig. 3c).

To date Gne is the only characterized BY-kinase substrate in *C. jejuni*, impeding analysis of other p-Tyr-containing proteins in this bacterium. Using 2D gel electrophoresis of *C. jejuni* outer membrane fractions followed by p-Tyr detection and mass spectrometry we identified CetB (Cj1189c), a protein involved in energy taxis and motility (18), as a tyrosine kinase substrate (Fig. S4b). CetB, cloned from *C. jejuni* 81-176, was expressed and purified using *E. coli* (Fig. S4c). As with Gne, CetB was also tyrosine phosphorylated by *E. coli* BY-kinases, reflecting the relaxed substrate specificity of bacterial tyrosine kinases (19). CetB was dephosphorylated on tyrosine only when H_2O_2 and cytochrome P450 were present (Fig. S4d). Many bacteria, including *E. coli,* do not express cytochrome P450 enzymes, but they contain heme peroxidases. A comparable decrease in p-Tyr was observed when purified recombinant UDP-glucose dehydrogenase (Ugd), a BY-kinase substrate expressed in *K. pneumoniae* and other bacteria, was treated with HRP in the presence of H_2O_2 (Fig. 3d, Fig. S4e). Ugd, which catalyzes the synthesis of UDP-glucuronic acid, is activated by phosphorylation of Tyr^{71}, and regulates capsule biosynthesis and colanic acid production (20). This result emphasizes the connection between H_2O_2-induced tyrosine dephosphorylation and attenuation of pathogenicity determinants.

H_2O_2-induced conversion of phosphotyrosine to PB-DOPA

To understand how tyrosine dephosphorylation occurs, we sought to identify the final product of this reaction by MS analysis of peptides derived from recombinant Gne or Ugd after exposure to H_2O_2 and HRP. In particular, both bacterial proteins contain phosphorylated key tyrosyl residues in their active site (Gne Tyr^{146}) or as cofactor affinity enhancer (Ugd Tyr^{71}) (20, 21), which are important for polysaccharide biosynthesis. Peptides containing these tyrosines were found to be oxidized by exogenous H_2O_2, leading to $^{\bullet}OH$-induced DOPA formation (Fig. 4a, b; Fig. S5a, b).

To ensure that the loss of tyrosine phosphorylation did not arise from variations in turnover of the limited pool of p-Tyr proteins, we determined concomitant loss of the p-Tyr signal and DOPA addition by performing analogous experiments using CjP450 (or HRP) together with a synthetic phosphopeptide (100% p-Tyr) comprising the sequence surrounding Gne Tyr^{146} in the presence of H_2O_2. The MS/MS spectra confirmed substantial loss of the phosphate group on tyrosine and matching DOPA modification, resulting in a net mass change of 63Da on modified tyrosines (Fig. 4c, d; Fig. S6a-d). Quantification revealed that the increase in DOPA signal in the peptide was accompanied by a decrease in the phosphorylated peptide (Fig. 4e).

A number of potential chemical mechanisms can be invoked to explain the conversion of p-Tyr to DOPA (Fig. S7). The source for hydroxylation could be water (Reaction 1) or H_2O_2 (Reactions 2 and 3). As $H_2{}^{18}O_2$ labeled DOPA (Fig. 4c, d; Fig. S6d), we ruled out Reaction 1. Reaction 2 would proceed via a 2-hydroxy-3,5-cyclohexadienone intermediate, whereas Reaction 3 would predict generation of a tyrosinyl radical intermediate (Fig. S7 boxed) (22, 23). The addition of free tyrosine to the oxidation reaction will discriminate between these two possibilities, as only a tyrosinyl radical intermediate will permit dityrosine formation. NanoLC-MS/MS analysis of the synthetic phosphopeptide, or of Gne and Ugd treated with H_2O_2 in the presence of L-tyrosine and CjP450 (or HRP) indicated dityrosine formation at active site tyrosines with a net mass change of 100Da (Fig. 4c, d, f, g; Fig. S6c, e, f). These results support Reaction 3 as the mechanism leading to oxidative phosphate removal and DOPA addition on tyrosine. Analysis of solvent accessibility surface area of modified tyrosines did not provide a clear link between surface exposure, tyrosinyl radical formation and subsequent DOPA modification (Fig. S8a, b), suggesting that the microenvironment surrounding certain tyrosines leads to specific, non-random oxidation events.

K. pneumoniae DOPA proteomics and computational chemistry approach

To assess bacterial PB-DOPA modifications globally, *K. pneumoniae* grown at 5% O_2 was exposed to a bolus of H_2O_2 or, separated by a filter, to 15-20nmol H_2O_2/h/mg protein continuously released by Cos-NOX4 cells, mimicking a rate of H_2O_2 release similar to stimulated IECs (24). Without employing any enrichment strategy MS/MS analysis revealed upregulation of the ROS scavengers superoxide dismutase (SOD, UniProtKB-M7QF58, 2-fold) and alkyl hydroperoxide reductase (AhpC 1.3-fold, AhpD 180-fold (by H_2O_2), AhpF 2-fold (by NOX4)), but not catalase (KatG). The relative abundance of PB-DOPA after treatment was increased (25-35%) over untreated conditions or when exposed to NOX4-deficient Cos-22^{phox} cells. Analysis of DOPA sites (Table S1) revealed that AhpC itself, a thiol-based peroxidase and the primary scavenger of low H_2O_2 concentrations in *E. coli* (25), was modified on Tyr^{157}, a residue previously identified as an AhpC phosphorylation site in *K. pneumoniae* and *E. coli* (9, 12). Tyr^{157} is located in the vicinity of the resolving Cys^{166} that reacts with Cys^{47} (26). We used molecular dynamics (MD) simulation of AhpC in different states to analyze disulfide bond connectivity, which revealed that the backbone regions move considerably closer together in the DOPA-modified AhpC dimer (Fig. 5a-c), which may affect turnover. Thus, H_2O_2 cannot only alter tyrosines in the catalytic center of enzymes involved in metabolic and virulence-associated pathways, but also hydroxylates AhpC, the initial antioxidant defense enzyme.

Proteomics data compiled in Table S1 indicate that DOPA addition on particular tyrosine residues, identified by us in *K. pneumoniae* or reported in *E. coli* K12 grown at 21% oxygen (27) match with p-Tyr modifications (9, 12). A frequently modified enzyme is glyceraldehyde-3-phosphate dehydrogenase (gapA, GAPDH-A), which is susceptible to DOPA modification on

Tyr^{312}, a residue identified also as phosphorylation site in *E. coli* (12). GAPDH, a glycolytic enzyme and H_2O_2 sensor with peroxidatic activity, contributes to colonization and invasion (28). Tyr^{312} in *K. pneumoniae* GAPDH (Tyr^{314} in human GAPDH) represents in unmodified form a critical residue in a proton-shuttle mechanism essential for the H_2O_2 sensitivity of the enzyme (29). MD simulations indicated that NAD^+ binding to phosphorylated Tyr^{312} lowered the desolvation energy (~10%), while subsequent DOPA modification decreased the electrostatic energy by approximately 40% and NAD^+ binding by 50% (Fig. 5d). The situation for human GAPDH is similar, although the $NADPH/NADP^+$ ratio for *K. pneumoniae* GAPDH would be higher. The direct conversion from unmodified Tyr^{312} to DOPA-Tyr^{312}, a process unlikely to occur in physiological conditions, would cause less structural change than a DOPA conversion from a phosphorylated residue (Fig. 5d). In contrast to the increased resistance of a human GAPDH Y314F mutant to oxidative inactivation (29), conversion of p-Tyr^{314} to DOPA will be comparable to exposure of wildtype GAPDH to 200µM H_2O_2 (29) and will not alter adaptation to oxidative stress. A subset of p-Tyr^{314} modified GAPDH might be present at any given time in mammalian tissues (30). Phosphorylated GAPDH will not require the proton relay for H_2O_2 sensitivity as the space for H_2O_2 interaction with Cys^{152} will be occupied by the phosphate group in p-Tyr^{314} and the creation of two hydrogen bonds between Cys^{152} and p-Tyr^{314} (Fig. 5e). Oxidative dephosphorylation and DOPA addition on Tyr^{314} will then alter NAD^+ affinity. These examples demonstrate that oxidative dephosphorylation and subsequent DOPA addition act as regulator of enzyme function, and that the outcome will differ depending on the structural and functional context. Improved techniques for detecting and stabilizing tyrosine modifications will permit discovering many more candidates for p-Tyr conversion, particularly in oxidative stress conditions.

Discussion

Phosphorylation-driven signaling networks are crucial for maintaining functional responses in all organisms. Similarly conserved is the release of diffusible mediators, in particular H_2O_2, for protection and adaptation. In mammalian systems thiol oxidation is a potent pathway modifier, often accelerating or causing disease when deregulated. In bacteria exposure to H_2O_2 concentrations in the nano to sub-micromolar range has been associated with oxidation of reactive cysteinyl residues and $[4Fe\text{-}4S]^{2+}$ clusters. Damaging irreversible modifications such as methionine oxidation and 3-chlorotyrosine formation were connected to the myeloperoxidase-H_2O_2-chloride axis and bacterial killing in the phagosome of neutrophils (5). Using a range of conditions including host-pathogen interaction models, constant exposure of bacteria to nmol H_2O_2 that mimics host epithelial H_2O_2 release during infection, or to a single bolus of H_2O_2, we report here disruption of p-Tyr signaling by oxidative p-Tyr conversion to DOPA (Fig. 5f).

Tyrosines in the vicinity of lysines, in particular in YXX(XX)K or KXXX(X)Y motifs, seem prone to hydroxylation or chlorination (27, 31), while also being preferred phosphorylation sites in *E. coli* proteins (12). These motifs are present in the DOPA-modified bacterial proteins Gne, Ugd, AhpC and GAPDH-A featured in this study. The nearby positive charge may favor the deprotonated form of tyrosine, facilitating phosphorylation and/or oxidative electron transfer. The presence of DOPA on proteins involved in ROS conversion (AhpC, SOD (27)) or in redox-sensitive processes (GAPDH-A), and the predicted structural change by DOPA incorporation pose the question of how their activity will be altered by Tyr hydroxylation. Redox-active PB-DOPA can generate radicals leading to enhanced oxidative damage, but has also been linked to peroxyl radical scavenging and antioxidant defense. The majority of bacterial DOPA-modified proteins identified to date are involved in carbohydrate metabolism (this study and (27)), which

constitutes also a preferred target for BY-kinase-mediated Tyr phosphorylation and a prerequisite for virulence determinants such as capsule and biofilm formation.

Besides H_2O_2 the availability of intrabacterial iron, peroxidase activity (e.g. via compound I) and a low oxygen environment were required for p-Tyr conversion to DOPA. The intestinal niche is largely devoid of oxygen except for a 70µm oxygenation zone maintained by capillary diffusion (13). Oxygen measurements by EPR or phosphorescence oximetry detected luminal P_{O2} levels of 1-40 mm Hg (≤5% O_2), depending on the section of the intestinal tract (32). Albeit lung P_{O2} levels are much higher, in pulmonary infection and in particular in cystic fibrosis anaerobic bacteria are frequently present, indicating a low oxygen environment. Propagation of bacteria in 21% oxygen does not reflect the *in vivo* situation for many mucosal pathogens. During oxidative stress modification of tyrosine residues to DOPA seems to occur frequently. PB-DOPA modifications were prominently associated with mitochondrial proteins in heart and brain tissues (33). The presence of H_2O_2 and transition metals in mitochondria creates an ideal environment for DOPA additions and modified proteins included SOD2, cytochrome c and ATPases (27, 33). Other DOPA-modified proteins were connected to oxidative stress pathways (NRF2, HSP90), the cytoskeletal regulatory network or are multifunctional adapters (14-3-3 family) (33). Many of the modified Tyr residues in these proteins are predicted phosphorylation sites. Our study connects oxidative stress to interference with p-Tyr signaling by directly converting tyrosine residues that are associated with the catalytic activity of enzymes. Oxidative stress may likely trigger additional modifications throughout the protein, for example methionine oxidations. Tyrosine phosphorylation promotes not only signaling responses, but affects also protein localization and protein-protein interactions, and it is expected that many DOPA modifications caused by oxidative stress or mitochondrial dysfunction will disrupt protein

networks, thereby altering numerous biological processes.

Materials and Methods

In Vitro Organ Culture (pIVOC*)* of human colon biopsies was performed as described (9). For infection studies fetal lung explant studies Sprague-Dawley® rats and ligated rabbit ileal loops from Chinchilla rabbits were used. Ethical approval by the respective overseeing bodies was obtained. Mass spectrometry, structural analysis and graphical representations are described in *SI Methods*. 3D-models of *K. pneumoniae* GAPDH-A (B5XS72_KLEP3) and *K. pneumoniae* AhpC (M7PUV9_KLEPN) were generated using the homology modeling program Modeller 9v14; molecular dynamics simulation and docking were performed with HADDOCK and evaluated in UCSF Chimera. Detailed procedures and biochemical/microbiological methods are described in *SI Appendix, SI Materials and Methods*.

Acknowledgments

We thank N. Corcionivoschi for his contributions, K. O'Neill and C. King for technical assistance, and C. Whitfield, P. Cossart, M. Baldus and J. Baugh for providing reagents, and P. Nagy for discussions. The work was supported by the National Children Research Centre (K/12/1; BB, UGK), Science Foundation Ireland (10/IN.1/B2988; UGK), and the COST Action BM1203 (UGK, LAJA). We would like to acknowledge staff and patients at the Natl Referral Center for Pediatric Gastroenterology, Our Lady's Children's Hospital Crumlin, Dublin, Ireland.

References

1. Cameron EA & Sperandio V (2015) Frenemies: Signaling and Nutritional Integration in Pathogen-Microbiota-Host Interactions. *Cell Host Microbe* 18(3):275-284.
2. Kamada N*, et al.* (2012) Regulated virulence controls the ability of a pathogen to compete with the gut microbiota. *Science* 336(6086):1325-1329.
3. Imlay JA (2013) The molecular mechanisms and physiological consequences of oxidative stress: lessons from a model bacterium. *Nat Rev Microbiol* 11(7):443-454.
4. Holmstrom KM & Finkel T (2014) Cellular mechanisms and physiological consequences of redox-dependent signalling. *Nat Rev Mol Cell Biol* 15(6):411-421.
5. Winterbourn CC & Kettle AJ (2013) Redox reactions and microbial killing in the neutrophil phagosome. *Antioxid Redox Signal* 18(6):642-660.
6. Wright CJ*, et al.* (2014) Characterization of a bacterial tyrosine kinase in Porphyromonas gingivalis involved in polymicrobial synergy. *MicrobiologyOpen* 3(3):383-394.
7. Chao JD, Wong D, & Av-Gay Y (2014) Microbial protein-tyrosine kinases. *J Biol Chem* 289(14):9463-9472.
8. Corcionivoschi N*, et al.* (2012) Mucosal reactive oxygen species decrease virulence by disrupting C jejuni phosphotyrosine signaling. *Cell Host Microbe* 12(1):47-59.
9. Lin MH*, et al.* (2009) Phosphoproteomics of K. pneumoniae NTUH-K2044 reveals a tight link between tyrosine phosphorylation and virulence. *Mol Cell Proteomics* 8(12):2613-2623.
10. Mancini S & Imlay JA (2015) The induction of two biosynthetic enzymes helps Escherichia coli sustain heme synthesis and activate catalase during hydrogen peroxide stress. *Mol Microbiol* 96(4):744-763.
11. Bilan DS*, et al.* (2013) HyPer3:a genetically encoded H_2O_2 probe with improved performance for ratiometric and fluorescence lifetime imaging. *ACS Chem Biol* 8:535-542.
12. Hansen AM*, et al.* (2013) The Escherichia coli Phosphotyrosine Proteome Relates to Core Pathways and Virulence. *PLoS Pathog* 9(6):e1003403.
13. Marteyn B, Scorza FB, Sansonetti PJ, & Tang C (2011) Breathing life into pathogens: the influence of oxygen on bacterial virulence and host responses in the gastrointestinal tract. *Cell Microbiol* 13(2):171-176.
14. Kroger C*, et al.* (2013) An infection-relevant transcriptomic compendium for Salmonella enterica Serovar Typhimurium. *Cell Host Microbe* 14(6):683-695.
15. Guengerich FP & Munro AW (2013) Unusual cytochrome p450 enzymes and reactions. *J Biol Chem* 288(24):17065-17073.
16. Alvarez LA*, et al.* (2013) Cj1411c encodes for a cytochrome P450 involved in Campylobacter jejuni 81-176 pathogenicity. *PLoS ONE* 8(9):e75534.
17. Prasad B, Mah DJ, Lewis AR, & Plettner E (2013) Water oxidation by a cytochrome p450: mechanism and function of the reaction. *PLoS ONE* 8(4):e61897.
18. Reuter M & van Vliet AH (2013) Signal balancing by the CetABC and CetZ chemoreceptors controls energy taxis in Campylobacter jejuni. *PLoS ONE* 8(1):e54390.
19. Shi L*, et al.* (2014) Evolution of bacterial protein-tyrosine kinases and their relaxed specificity toward substrates. *Genome Biol Evol* 6(4):800-817.
20. Lacour S, Bechet E, Cozzone AJ, Mijakovic I, & Grangeasse C (2008) Tyrosine phosphorylation of the UDP-glucose dehydrogenase of Escherichia coli is at the crossroads of colanic acid synthesis and polymyxin resistance. *PLoS ONE* 3(8):e3053.

21. Chen YY, Ko TP, Lin CH, Chen WH, & Wang AH (2011) Conformational change upon product binding to K. pneumoniae UDP-glucose dehydrogenase: a possible inhibition mechanism for the key enzyme in polymyxin resistance. *J Struct Biol* 175(3):300-310.
22. Houee-Levin C*, et al.* (2015) Exploring oxidative modifications of tyrosine: an update on mechanisms of formation, advances in analysis and biological consequences. *Free Radic Res* 49(4):347-373.
23. Nagy P, Lechte TP, Das AB, & Winterbourn CC (2012) Conjugation of glutathione to oxidized tyrosine residues in peptides and proteins. *J Biol Chem* 287(31):26068-26076.
24. Martyn KD, Frederick LM, von Loehneysen K, Dinauer MC, & Knaus UG (2006) Functional analysis of Nox4 reveals unique characteristics compared to other NADPH oxidases. *Cell Signal* 18(1):69-82.
25. Mishra S & Imlay J (2012) Why do bacteria use so many enzymes to scavenge hydrogen peroxide? *Arch Biochem Biophys* 525(2):145-160.
26. Parsonage D, Karplus PA, & Poole LB (2008) Substrate specificity and redox potential of AhpC, a bacterial peroxiredoxin. *Proc Natl Acad Sci U S A* 105(24):8209-8214.
27. Lee S*, et al.* (2010) The first global screening of protein substrates bearing protein-bound 3,4-Dihydroxyphenylalanine in Escherichia coli and human mitochondria. *J Proteome Res* 9(11):5705-5714.
28. Pancholi V & Chhatwal GS (2003) Housekeeping enzymes as virulence factors for pathogens. *Int J Med Microbiol : IJMM* 293(6):391-401.
29. Peralta D*, et al.* (2015) A proton relay enhances H2O2 sensitivity of GAPDH to facilitate metabolic adaptation. *Nat Chem Biol* 11(2):156-163.
30. Guo A*, et al.* (2008) Signaling networks assembled by oncogenic EGFR and c-Met. *Proc Natl Acad Sci U S A* 105(2):692-697.
31. Bergt C, Fu X, Huq NP, Kao J, & Heinecke JW (2004) Lysine residues direct the chlorination of tyrosines in YXXK motifs of apolipoprotein A-I when hypochlorous acid oxidizes high density lipoprotein. *J Biol Chem* 279(9):7856-7866.
32. Albenberg L*, et al.* (2014) Correlation between intraluminal oxygen gradient and radial partitioning of intestinal microbiota. *Gastroenterology* 147(5):1055-1063 e1058.
33. Zhang X*, et al.* (2010) Endogenous 3,4-dihydroxyphenylalanine and dopaquinone modifications on protein tyrosine: links to mitochondrially derived oxidative stress via hydroxyl radical. *Mol Cell Proteomics* 9(6):1199-1208.
34. Turriziani B*, et al.* (2014) On-Beads Digestion in Conjunction with Data-Dependent Mass Spectrometry: A Shortcut to Quantitative and Dynamic Interaction Proteomics. *Biology* 3(2):320-332.
35. Renault M*, et al.* (2012) Cellular solid-state nuclear magnetic resonance spectroscopy. *Proc Natl Acad Sci U S A* 109(13):4863-4868.
36. Phillips JC*, et al.* (2005) Scalable molecular dynamics with NAMD. *J Comput Chem* 26(16):1781-1802.
37. de Vries SJ, van Dijk M, & Bonvin AM (2010) The HADDOCK web server for data-driven biomolecular docking. *Nat Protoc* 5(5):883-897.
38. van Dijk AD & Bonvin AM (2006) Solvated docking: introducing water into the modelling of biomolecular complexes. *Bioinformatics* 22(19):2340-2347.
39. Oh E & Jeon B (2014) Role of Alkyl Hydroperoxide Reductase (AhpC) in the Biofilm Formation of *Campylobacter jejuni*. *PLoS ONE* 9(1):e87312.

Figure Legends

Figure 1. Mucosal H_2O_2 leads to tyrosine dephosphorylation in intestinal bacteria

(a) H_2O_2 release by IECs (HCT-8) following exposure to enteric bacteria (+/- DPI or catalase addition) and by Cos-NOX4 cells separated from bacteria by a filter (*K. pneum*.-blue, *L. monocyt*.-grey, *S. typhim*.-green). (b) H_2O_2 release by colonic biopsies after infection with *L. monocytogenes* (patients P1, P2). Control is DPI preincubation of biopsies. (c) Carbonylation of rabbit ileal loop tissues after injection with PBS, *L. monocytogenes* (1.5h) or *C. jejuni* (3h). Scale bar 25µm. (d, e) Anti-p-Tyr immunoblots of lysates derived from extracellular bacteria exposed to IEC (d) or Cos-NOX4 (e) for 3h (see a). (f) Anti-p-Tyr immunoblot of extracellular *L. monocytogenes* after exposure to biopsies (see b) (3h). Starting culture is used for comparison. (g) Anti-p-Tyr immunoblot of *L. monocytogenes* or *C. jejuni* recovered from the ileal loop lumen.

Figure 2. Oxygen and iron availability affect oxidative dephosphorylation of tyrosines

(a, b) Anti-p-Tyr immunoblots of bacteria cultured in 5% or 21% O_2 (a) or in low or high iron conditions at 5% O_2 (b) prior to 0.7mM H_2O_2 addition (3h). (c) Quantification of Fe^{3+} vs Fe^{2+} in indicated bacteria co-cultured with HCT-8 cells (+/- DPI pretreatment). (d) Quantification of carbonyl formation in *C. jejuni* or *K. pneumoniae* protein extracts after HCT-8 co-culture. Error bars represent SEM and asterisks indicate significance (*** $p \leq 0.001$; ** $p \leq 0.01$ and * $p \leq 0.05$).

Figure 3. Cytochrome P450 or peroxidases are required for oxidative phosphate removal

(a) Anti-p-Tyr immunoblot of *C. jejuni* strains with or without exposure to H_2O_2. *C. jejuni* 81-176 (WT) was compared to *C. jejuni* Δ*cjj81176_1410* (Δ*P450*), to the P450 reconstituted strain (Δ*P450::P450*) or to *C. jejuni* Δ*P450* reconstituted with P450 active site cysteine mutant (Δ*P450::P450 C399F*). Blots were reprobed with anti-P450 antibody. (b) Tyrosine dephosphorylation of *C. jejuni* Gne by *C. jejuni* cytochrome P450 in the presence or absence of

1mM H_2O_2. Catalase and dithionite served as controls for H_2O_2 and P450 activity, respectively. Anti-p-Tyr, anti-His tag and anti-P450 immunoblots are shown. (c) Tyrosine dephosphorylation of Gne by HRP in the presence or absence of 1mM H_2O_2. (d) Tyrosine dephosphorylation of *E. coli* Ugd by HRP in the presence or absence of 1mM H_2O_2.

Figure 4. DOPA modification displaces phosphate via tyrosinyl radical formation

(a, b) Oxidized over unmodified peptide intensities of (a) the Gne peptide (aa 117-150) containing Tyr^{146} and of (b) the Ugd peptide (aa 68-88) containing Tyr^{71} in the MS spectra. Y_{ox} indicates DOPA-modified tyrosine. Localization of oxidized tyrosine residues is shown in worm-style with width proportional to residue accessibility and in the peptide sequence. (c, d) MS spectra of a synthetic phosphotyrosine peptide (biotin-INPpYGR) after treatment with 1mM H_2O_2 and either (c) CjP450 or (d) HRP. The starting phosphorylated peptide is in black, DOPA in red, dityrosine formation in purple and ^{18}O oxidation in cyan. The reactions leading to each modification are indicated. (e) Quantification of pY vs Y_{ox} in the synthetic INPpYGR peptide upon exposure to 1mM H_2O_2 +/- HRP using MS/MS. (f, g) Isotopic peak MS spectra indicating dityrosine formation (purple) for tryptic peptides derived from Gne (f) or Ugd (g) following treatment as indicated.

Figure 5. DOPA modification on oxidative stress-associated *K. pneumoniae* proteins

(a-c) AhpC 3D model depicting Tyr^{157} in relation to Cys^{47} and Cys^{166} in unmodified (a), p-Tyr^{157} (b) and DOPA-Tyr^{157} (c) conformation. Cys-Cys distances indicated in Angström. (d) Binding energy for NAD^+ to GAPDH (*K. pneum.* Tyr^{312}, human Tyr^{314}) in unmodified, phosphorylated, p-Tyr to DOPA, or unmodified to DOPA form. Van der Waals energy (hatched), electrostatic energy (white) and desolvation energy (black). (e) Comparison of unmodified, p-Tyr^{314} and DOPA-Tyr^{314} human GAPDH. Tyr^{314} is shown space filling, side chains are sticks, hydrogen

bonds are dashed lines in cyan indicated with arrows. (f) Schematic representation of the key reactions leading to oxidative dephosphorylation of bacterial tyrosyl residues and conversion to DOPA.

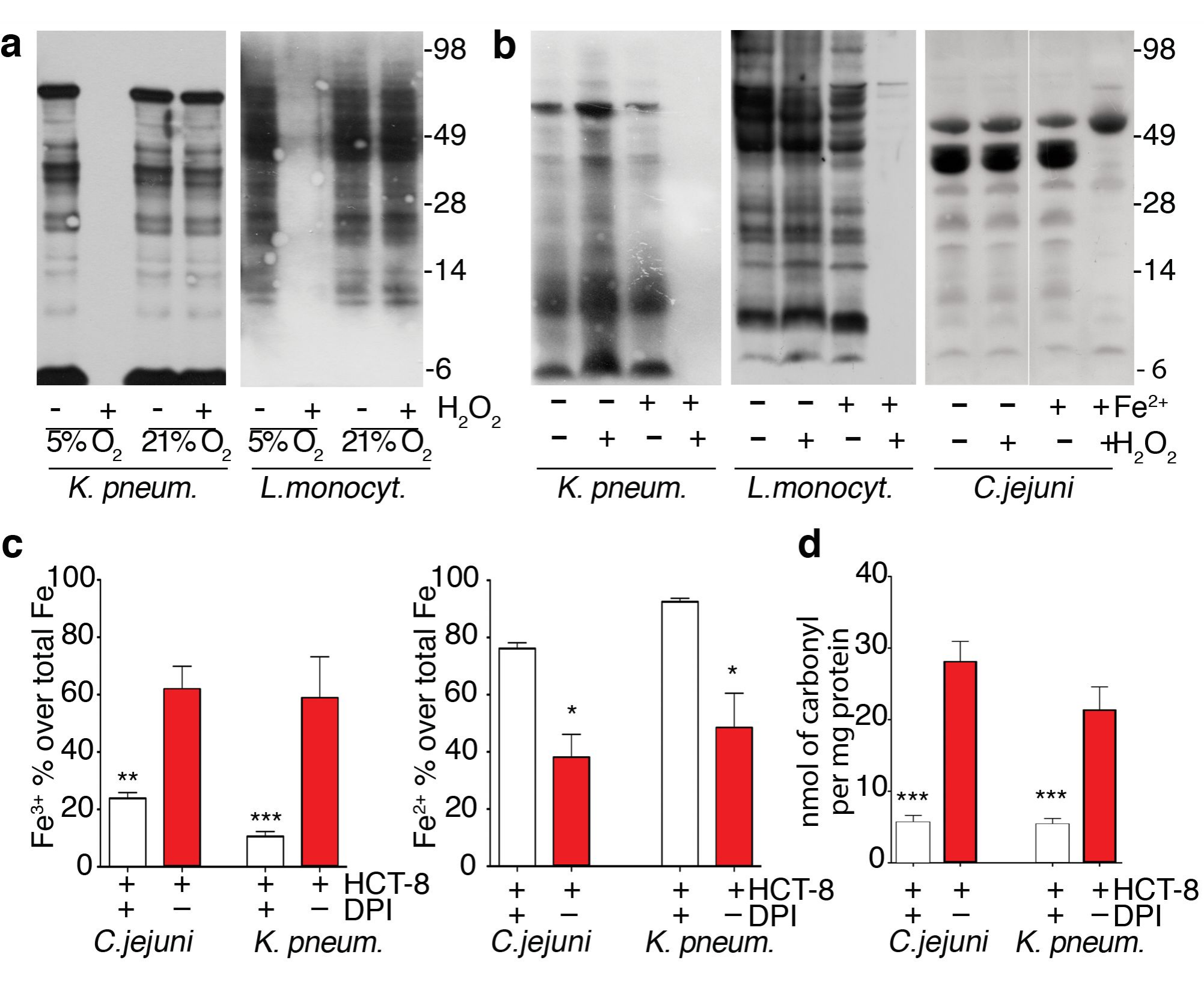
a
b
c
d
-98
-49
-28
-14
-6
- 6
H2O2
Fe2+
5% O2
21% O2
K. pneum.
L.monocyt.
C.jejuni
Fe3+ % over total Fe
Fe2+ % over total Fe
nmol of carbonyl per mg protein
HCT-8
DPI
**
***
*

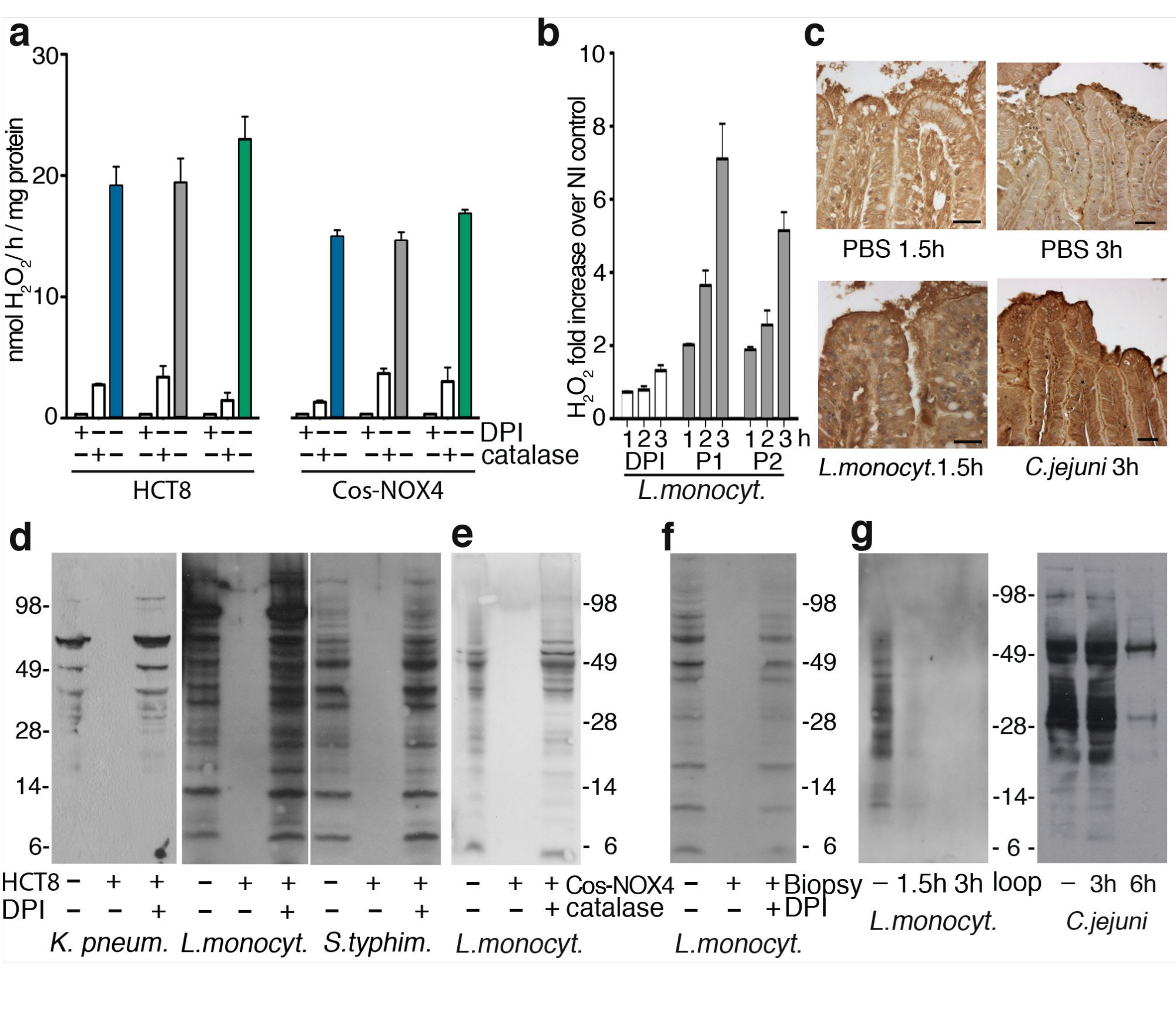
a
nmol H_2O_2/ h / mg protein
30
20
10
0
+ − − + − − + − − DPI
− + − − + − − + − catalase
HCT8
Cos-NOX4
b
H_2O_2 fold increase over NI control
10
8
6
4
2
0
1 2 3 1 2 3 1 2 3 h
DPI P1 P2
L.monocyt.
c
PBS 1.5h
PBS 3h
L.monocyt.1.5h
C.jejuni 3h
d
98-
49-
28-
14-
6-
HCT8 − + + − + + − + + DPI
DPI − − + − − + − − +
K. pneum. L.monocyt. S.typhim.
e
-98
-49
-28
-14
- 6
− + + Cos-NOX4
− − + catalase
L.monocyt.
f
-98
-49
-28
-14
- 6
− + + Biopsy loop
− − + DPI
L.monocyt.
g
-98-
-49-
-28-
-14-
- 6 -
− 1.5h 3h
− 3h 6h
L.monocyt.
C.jejuni

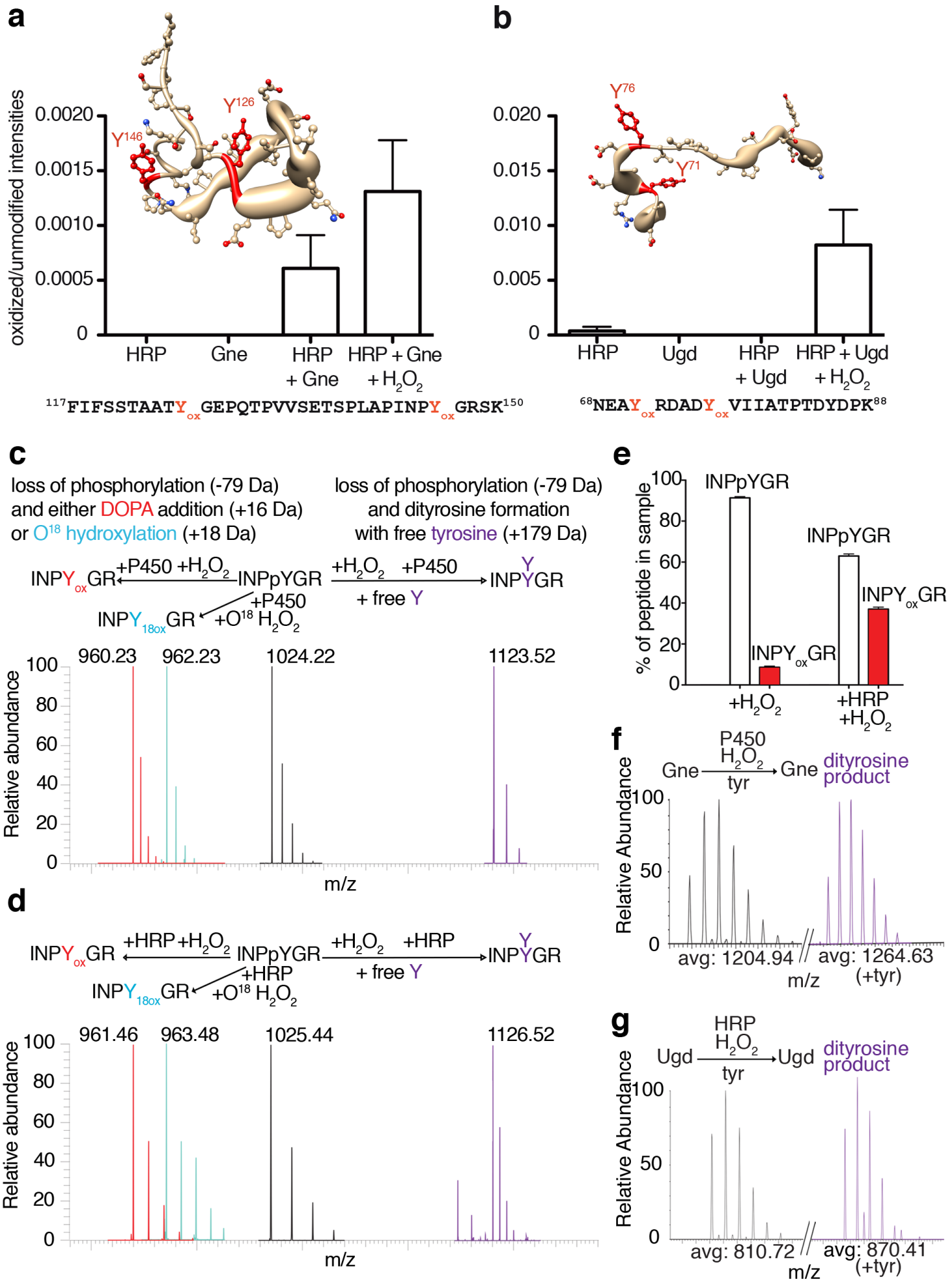
a
oxidized/unmodified intensities
0.0020
0.0015
0.0010
0.0005
0
Y126
Y146
HRP
Gne
HRP + Gne
HRP + Gne + H2O2
117FIFSSTAATYoxGEPQTPVVSETSPLAPINPYoxGRSK150
b
0.020
0.015
0.010
0.005
0
Y76
Y71
HRP
Ugd
HRP + Ugd
HRP + Ugd + H2O2
68NEAYoxRDADYoxVIIATPTDYDPK88
c
loss of phosphorylation (-79 Da) and either DOPA addition (+16 Da) or O18 hydroxylation (+18 Da)
loss of phosphorylation (-79 Da) and dityrosine formation with free tyrosine (+179 Da)
INPYoxGR
+P450 +H2O2
INPpYGR
+H2O2 +P450
+ free Y
INPYGR
+P450
INPY18oxGR
+O18 H2O2
960.23
962.23
1024.22
1123.52
Relative abundance
m/z
d
INPYoxGR
+HRP +H2O2
INPpYGR
+H2O2 +HRP
+ free Y
INPYGR
+HRP
INPY18oxGR
+O18 H2O2
961.46
963.48
1025.44
1126.52
Relative abundance
m/z
e
% of peptide in sample
INPpYGR
INPYoxGR
+H2O2
+HRP +H2O2
f
P450 H2O2
Gne
tyr
Gne
dityrosine product
Relative Abundance
avg: 1204.94
avg: 1264.63 (+tyr)
m/z
g
HRP H2O2
Ugd
tyr
Ugd
dityrosine product
Relative Abundance
avg: 810.72
avg: 870.41 (+tyr)
m/z

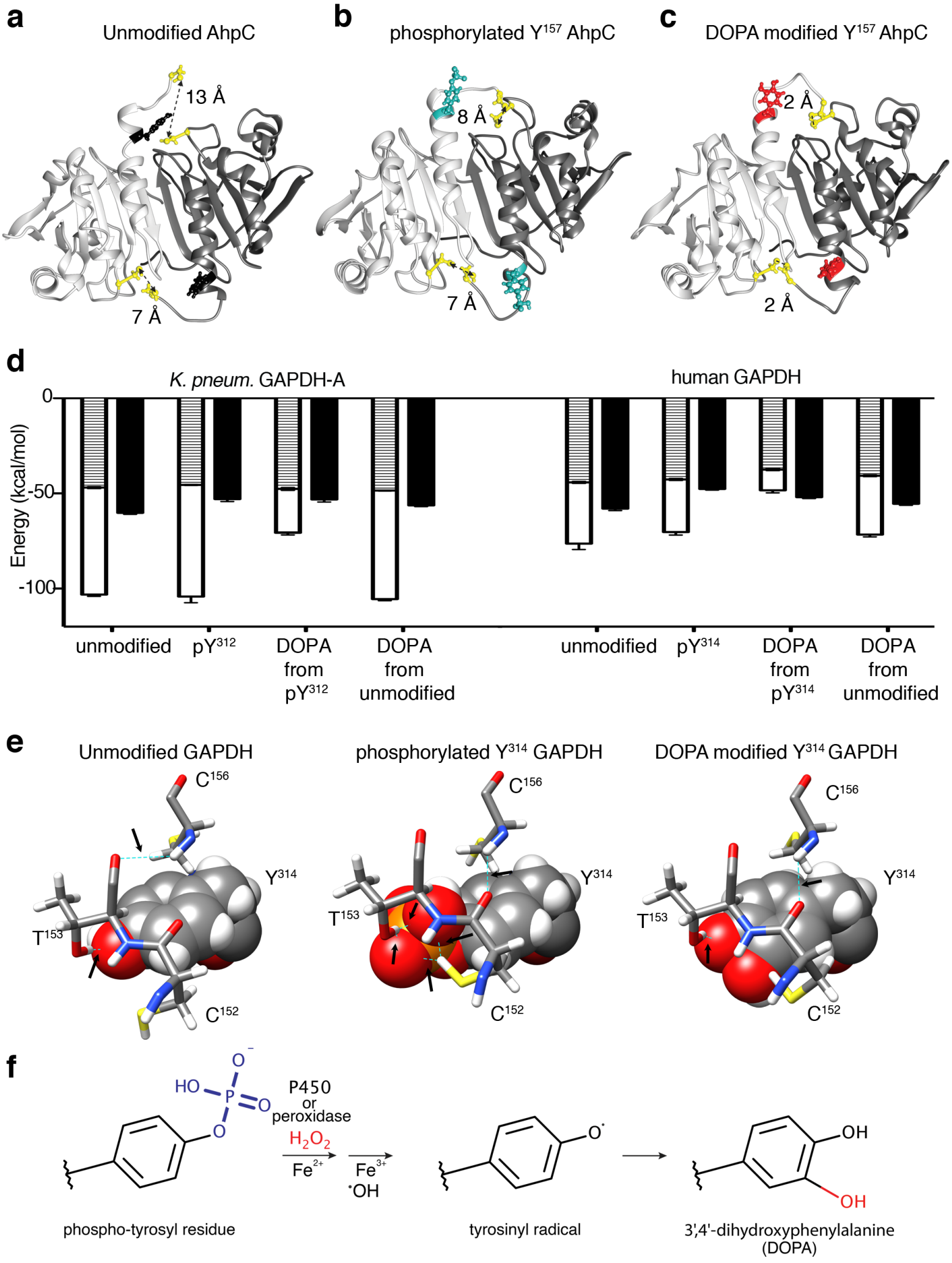
a
Unmodified AhpC
13 Å
7 Å
b
phosphorylated Y157 AhpC
8 Å
7 Å
c
DOPA modified Y157 AhpC
2 Å
2 Å
d
K. pneum. GAPDH-A
human GAPDH
Energy (kcal/mol)
0
-50
-100
unmodified
pY312
DOPA from pY312
DOPA from unmodified
unmodified
pY314
DOPA from pY314
DOPA from unmodified
e
Unmodified GAPDH
phosphorylated Y314 GAPDH
DOPA modified Y314 GAPDH
C156
Y314
T153
C152
f
HO
P
O
P450 or peroxidase
H2O2
Fe2+
Fe3+
·OH
phospho-tyrosyl residue
tyrosinyl radical
OH
3',4'-dihydroxyphenylalanine (DOPA)

Supplementary Information

NADPH oxidase-derived H_2O_2 subverts pathogen signaling by oxidative phosphotyrosine conversion to PB-DOPA

Luis AJ Alvarez, Lidija Kovačič, Javier Rodríguez, Jan-Hendrik Gosemann, Malgorzata Kubica, Gratiela Pircalabioru, Florian Friedmacher, Ada Cean, Alina Ghişe, Mihai B Sărăndan, Prem Puri, Simon Daff, Erika Plettner, Alexander von Kriegsheim, Billy Bourke, Ulla G Knaus

Supplementary Materials and Methods

Bacteria, cell lines and culture conditions

The following bacterial strains were used: *Campylobacter jejuni* 81-176 was cultured on Mueller-Hinton Agar, then sub-cultured in bi-phasic media containing RPMI 1640 supplemented with 3% FBS for infection studies. *Listeria monocytogenes* EGDe (gift from P. Cossart) was cultured on Brain Heart Infusion (BHI) media, *Salmonella enterica* subsp. *enterica* serovar Typhimurium ATCC 14028™, *Klebsiella pneumoniae* subsp. *pneumoniae* ATCC 700603™ was cultured on Luria-Bertani media; if not indicated otherwise all bacterial strains were grown at 37ºC in microaerophilic conditions (5% CO_2, 5% O_2, 90% N_2), approx. 40mm Hg. *Streptococcus pneumoniae* ATCC 6305™ was grown on Todd Hewitt media at 37ºC overnight, then subcultured 1:10 (v/v) in fresh media and grown until OD_{600} =0.2 to ensure bacteria were in the exponential phase in order to prevent endogenous H_2O_2 production. HCT-8 cells (ATCC CCL-244^{TM}) were maintained in RPMI 1640 with 10% FBS. A rat alveolar macrophage cell line ATCC CRL-2192^{TM}, kindly provided by J. Baugh, was grown in Ham's F12K media supplemented with 15% FBS. Cells were grown at 21% O_2, 5% CO_2 and transferred to

microaerophilic conditions for infection 3h prior to the experiment. All treatments were performed at microaerophilic conditions if not stated otherwise.

Microbiological methods

Invasion and adhesion assays were performed as previously reported (8). Bacterial cell viability was assessed using the XTT (2,3-Bis-(2-Methoxy-4-Nitro-5-Sulfophenyl)-2*H*-Tetrazolium-5-Carboxanilide) assay (Life Technologies). For all *in vitro* experiments bacteria were exposed at time zero once to 0.7mM H_2O_2 in media, except for *C. jejuni* (5mM H_2O_2), and analyzed after the indicated time periods (max up to 3h, except for *C. jejuni* up to 8h). A bolus of 0.5mM H_2O_2 to *E. coli* in LB medium will result in an initial concentration of less than 3μM H_2O_2 inside *E. coli* with a complete extracellular H_2O_2 clearance in 1.5-2h (10, 11).

Molecular Biology

Gene deletion and reconstitution for cytochrome P450 encoded by *cjj81176_1410* (*C. jejuni* 81-176, NCBI: YP_001001066.1) has been described (16). Mutants were generated by site-directed mutagenesis using the QuikChange Lightning Site-Directed Mutagenesis Kit (Agilent Technologies). The PRY107 plasmid (KanR) was used as template followed by natural transformation of *C. jejuni* 81-178 Δ*P450* strain to give *C. jejuni* 81-176 Δ*P450*::*P450C339F* strain. The oligonucleotides used were C339FF (gtaggggaaagaatttgtatagga) and C339FR (catccccttttcttaaacatatcct). Mutants were generated by site-directed mutagenesis using the QuikChange Lightning Site-Directed Mutagenesis Kit (Agilent Technologies). Gne epimerase (*cjj81176_1148*) was amplified by PCR with primers GneRhaF (catcatcaccaccatcacaaaattcttattagcggtggt) and GneRhaR

(gtggcggccgctctattaacactgtttttcccaatcaaaacg) using Velocity™ DNA polymerase (MyBio, Ireland). CetB (*cjj81176_1204*) was amplified using primers CetBRhaF (catcatcaccaccatcacatgtcaagagaaatttttttacaa) and CetBRhaR (gtggcggccgctctattatttagcttcttgaagaga). Chloramphenicol (20µg/ml) and kanamycin (50µg/ml) were used for selection. For expression of His-tagged CetB the Expresso® Rhamnose Cloning and Protein Expression Kit (Lucigen Corp.) was used following the manufacturer's instructions. His-tagged Gne and Ugd (Ugd kindly provided by C. Whitfield) were cloned into a pet27b+ vector and transformed into BL21Star(DE3) CE1535 strain (kindly provided by M. Baldus) (34).

Protein purification

E. coli cultures were grown in LB broth containing 30µg/ml kanamycin at 36°C to OD_{600} =0.5 before harvesting. Either L-rhamnose or IPTG was added to the culture in a final concentration of 0.2% (w/v) and *E. coli* was grown for additional 18h or 6h at 36°C. *E. coli* lysates containing 50mM Hepes pH7.5, 0 or 25mM imidazole and EDTA-free protease inhibitors cocktail were loaded onto a HisTrap™ FF column or complete His-Tag column, washed with 0 or 25mM imidazole and eluted with 250-500mM imidazole on an AKTApurifier. Collected samples were desalted and concentrated on Centricon 10kDa membranes. *C. jejuni* cytochrome P450 purification was described elsewhere (16). Protein identity and purity were confirmed by Coomassie blue staining and immunoblotting. Bacterial proteins expressed and isolated from *E. coli* were always purified in tyrosine phosphorylated form, albeit the extent of p-Tyr was not quantified.

Co-culture of bacteria with cells in normal or iron-modified conditions

Bacteria in RPMI 1640 containing 3% FBS (OD_{600} =0.4; 10^7 bacteria, 1 ml) were incubated with HCT-8 cells at 37°C in microaerophilic conditions with MOI 50. HCT-8 cells were either pretreated with DPI for 20 min (25μM) followed by washout or catalase was added. Bacteria were not exposed to DPI except when indicated. Non-adherent, extracellular bacteria were removed by centrifugation of media (3300g, 5 min), and were used for immunoblotting. Viable counts were performed for inocula to ensure that comparable numbers of live bacteria were present for each bacterial strain. Exposure of bacteria to H_2O_2 released by Cos cells stably expressing the constitutively active NOX4-$p22^{phox}$ complex or as negative control Cos cells expressing only $p22^{phox}$ was performed using Boyden chambers. Cells in DMEM, 10% FBS medium were seeded into the bottom chamber 24h before start of the experiment and then moved to microaerophilic conditions for 3h in fresh DMEM, 3% FBS. Bacteria grown in microaerophilic conditions were resuspended in 5% O_2 conditioned DMEM with 3% FBS, placed on top of the filter (3μm pore size) and incubated for 3h. Bacteria were harvested from the filter for analysis.

Quantification of protein phosphotyrosine levels in modified iron conditions

C. jejuni 81-176, *L. monocytogenes* EGDe and *K. pneumoniae* were grown microaerophilic in LB medium, diluted into iron-free minimal essential media 1:20 and grown to mid-log phase (OD_{600}=0.2-0.3). Bacteria were collected by centrifugation (5000 rpm, 10 min) and diluted to OD_{600}=0.2 in MEM. Iron (II) sulfate (40μM) was added as indicated and cultures were grown microaerophilic until OD_{600}=0.5 was reached. To *C. jejuni* 81-176 cultures 5mM H_2O_2 was added and the growth continued microaerophilic for 8h. *L. monocytogenes* and *K. pneumoniae* cultures were exposed to 0.7mM H_2O_2 for 3h in microaerophilic conditions. Bacteria were then

diluted to OD_{600}=0.2, collected by centrifugation, washed twice with 25mM Tris-HCl, resuspended in 30µl Laemmli buffer (Sigma, UK) and heated for 5 min at 95^0C. Boiled samples were loaded on 10% SDS-PAGE gels, separated by electrophoresis and immunoblotted. The control samples followed an identical protocol without supplemental iron or added H_2O_2. Equal protein loading of bacterial lysates and similar protein expression patterns were assessed for every treatment modality by Coomassie blue staining.

***Ex vivo* analysis**

Polarized In Vitro Organ Culture (pIVOC) - pIVOC experiments of colon biopsies were performed as described (8). Bacterial infections were conducted using microaerophilic preconditioned media or buffers. *L. monocytogenes* was added at a final OD_{600} =0.2 to the apical side of biopsies and H_2O_2 release was measured at different time points as described in Biochemical Methods. Controls were either non-infected biopsies or biopsies pretreated with 20µM DPI for 20 min with washout before addition of *C. jejuni* or *L. monocytogenes*. Fully informed consent was obtained from parents and where appropriate, children. Ethical permission was obtained from the Ethics Committee of Our Lady's Childrens' Hospital Crumlin, Ireland.

Rat lung cultures - Sprague-Dawley® rats (Harlan Laboratories, Shardlow, UK) were kept in SPF conditions. Timed mating was performed and fetuses were delivered via caesarean section and sacrificed by decapitation on E21.5. Whole fetal lungs were dissected under sterile conditions. The harvested lungs were kept in ice-cold DMEM/F12 media for maximal 1h. The lungs were then washed twice in HBSS Ca^{2+} Mg^{2+} before being transferred to a transwell insert containing warm DMEM/F12 with 3% FBS, followed by incubation in 5% CO_2, 21% O_2 at 37ºC overnight. Next morning bacteria grown at 5% O_2 were introduced into the lungs under a dissecting

microscope by using a Teflon tip G25 cannula inserted into the intact trachea. After 2h and 4h of incubation the bronchoalveolar fluid was recovered and centrifuged. The supernatant was used for determination of H_2O_2. After H_2O_2 measurement recovered bacteria were lysed and analyzed by immunoblotting. All animal procedures were performed after ethical approval from the Royal College of Surgeons in Ireland and licensed by the Department of Health and Children, Ireland.

***In vivo* analysis**

Ligated rabbit ileal loops - Female rabbits (Chinchilla breed) were starved for 2h prior to infection. Anesthesia was performed iv with ketamine (35mg/kg) and xylazine (5mg/kg). The incision line was injected subcutaneously with 2 ml xylazine 1%. After laparotomy four ileal loops (5 cm in length) were isolated and ligated. The loops were injected with either PBS, *C. jejuni* 81-176 or *L. monocytogenes* EDGe using 1 ml of culture at OD_{600}=0.3 in PBS (pH7.4). For each microorganism 3 rabbits were used. After closure of the abdomen rabbits were placed in cages for 180-360 minutes (*C. jejuni*) or 90-180 minutes (*L. monocytogenes*). Rabbits were sacrificed by intravenous injection of sodium pentobarbital (120mg/kg). Fluid accumulated in each loop was collected separately and spun at 1000 rpm for 5 min to remove debris, followed by centrifugation at 5000 rpm to collect bacteria. Subsequently, the segments were fixed in Carnoy reagent (60% ethanol/30% chloroform/10% glacial acetic acid) for 24h at 4˚C. The experiments were performed under the supervision of the Romanian National Sanitary Veterinary Agency (Law 471/2002, Government ordinance 37/2002) with approval of the Ethics Committee of Banat's University of Agricultural Sciences and Veterinary Medicine, King Michael I of Romania, Timisoara.

General Materials

The following antibodies were used: anti-phosphotyrosine (sc-7020, Santa Cruz); anti-His antibody (sc-53073, Santa Cruz); anti-*Campylobacter* antibody (sc-58100, Santa Cruz) and anti-*Campylobacter* serum (8); anti-p22^{phox} (mAb 449, gift from D. Roos); anti-gp91^{phox} (NOX2; BD Biosciences); anti-*Campylobacter* P450 (16); Difco™ Listeria O Antisera Types 1, 4 and Poly (BD Biosciences); diphenyleneiodonium chloride (DPI, 15-25 μM, 15-30 min preincubation followed by PBS wash), bovine liver catalase (300U/ml); HRP Type II (P8250 Sigma; 400U/ml); sodium dithionite (used in excess); L-tyrosine (47 μM for Gne and 174 μM for Ugd experiments according to Tyr content).

Biochemical methods

H_2O_2 production was measured using Amplex UltraRed/HRP (Life Sciences) without sodium azide addition. Accumulation of fluorescent product (RFU) was measured at indicated time points, H_2O_2 was determined via a standard curve obtained in the same conditions, and values were adjusted to the protein content of the sample (IEC, biopsies). Values are expressed as nmol H_2O_2/h/mg protein. Catalase and diphenyleneiodonium were used as controls for H_2O_2 generation and flavoenzyme involvement, respectively. Cos-NOX4 cells were used as continuous physiological H_2O_2 generating system that will not necessitate contact between bacteria and cells (8). For Cos-NOX4 cells H_2O_2 was measured on top of the Boyden chamber filter (location of bacteria). For the pIVOC system the Amplex UltraRed/HRP solution was mixed at every time point 1:1 with media (50 μl of 500 μl total) collected at the apical side of the pIVOC followed by fluorescence readings (λ_{ex} = 550 nm; λ_{em} = 580nm) on a Synergy Mx fluorimeter with measurements performed 60, 120 and 180 min after the addition of bacteria.

Non infected control tissues were set as baseline and fluorescence was plotted as % change over baseline.

Immunoblotting, 2D electrophoresis and the corresponding MS/MS analysis were performed as described (8). For *in vitro* assays, recombinant tyrosine phosphorylated proteins were treated with 1mM H_2O_2 for 1h at 37ºC in Tris pH7 buffer in a 1:20 enzyme to substrate ratio (HRP/cjP450:Ugd/Gne) before EndoLysC digestion. A biotinylated, 100% phosphotyrosine containing synthetic peptide (biotin-INPpYGR; Biomatik, DE) at 95% purity was used for MS/MS analysis. 0.5mM peptide was bound to agarose streptavidin beads (Millipore) prior to exposure to 1mM H_2O_2 and 5 U/ml of HRP, or 3µl of purified cjP450 in a 60 µl reaction for 1h at 37º. For the dityrosine experiment with free tyrosine in P450 reactions the peptide was not bound to streptavidin beads. A commercial iron determination assay (ABCAM ab83366) was used to quantify the intracellular ratio of Fe^{2+} vs Fe^{3+} in bacteria. For carbonyl detection in bacterial protein extracts an assay kit (ABCAM ab126287) was used.

Mass spectrometry, structural analysis and graphical representations

Mass spectrometry analysis was performed as described in (35). Protein samples were digested with EndoLysC, while synthetic peptides were separated from streptavidin beads and directly analyzed in mass spectrometry. Proteolytic or synthesized peptides were analyzed on a Q-Exactive mass spectrometer connected to an Ultimate Ultra3000 chromatography system incorporating an autosampler (both Thermo Scientific, Germany). Proteolytic or synthesized peptides for each sample (5µL) were applied to a homemade column (100mm length, 75µm inside diameter [i.d.]) (packed with 1.9µm ReprosilAQ C18 by Dr. Maisch, Germany) and separated using either a 40 min (for purified proteins and peptides) or 240 min (for whole-

proteome samples) reverse-phase acetonitrile gradient (3%–32% acetonitrile) with a 250nL/min flow rate. The mass spectrometer was operated in positive ion mode with a capillary temperature of 220 °C and a 2000 V potential applied to the column. The intensities ratios of the modified peptides over the base peptides was used for normalization and expressed as fold increase over the untreated samples.

C. jejuni 81-176 Gne UDP-glucose 4-epimerase (A1W0B7) and *E.coli* Ugd glucose 6-dehydrogenase (P76373) were modelled using SWISS-MODEL workspace with UDP-galactose-4-epimerase from *Aspergillus nidulans* (PDB: 4lis.1) and UDP-glucose dehydrogenase from *K. pneumoniae* (PDB: 3pjg.1) as templates. UCSF Chimera was used for protein visualization. The MS/MS package in UCSF Chimera was used for the solvent-accessibility surface area calculations and the render by attribute is in Worm style (https://www.cgl.ucsf.edu/chimera/docs/ContributedSoftware/render/render.html#worms).

Chemical reactions were drawn with the sketch module in Marvin Beans Version 15.7.13.0, (https://www.chemaxon.com). For Figure 4c-d, chromatograms of the 2 charged peptides were used for the indicated experiments and combined in a single graph. For easier calculation of mass changes, the peaks were labeled with the 1 charged equivalent mass in the figure.

Molecular dynamics simulation and docking

Three-dimensional models of *K. pneumoniae* GAPDH-A (B5XS72_KLEP3) were generated using the homology modeling program Modeller 9v14 (http://www.salilab.org/modeller/) with structures of human or *E. coli* GAPDH serving as initial template (PDB ID: 1U8F and 1S7C, respectively). An AhpC structure from *E. coli* (PDB: 4QL7) was used for *K. pneumoniae* AhpC (M7PUV9_KLEPN). Putative structural changes caused by phosphorylation and subsequent

DOPA modification on Tyr^{157} in AhpC (*K. pneumoniae*) or on Tyr^{312} in GAPDH-A (*K. pneumoniae*) and on Tyr^{314} in human GAPDH respectively were simulated using a NAMD 2.11 program (36), http://www.ks.uiuc.edu/Research/namd/) plug-in in VMD v1.9.2 (http://www.ks.uiuc.edu/Research/vmd/). For AhpC simulation the dimer was used as a starting unit, all disulfide bridges were removed, all atoms were used and all movements were followed for 20 ps. In the AhpC dimer both Tyr^{157} residues were either unmodified, phosphorylated or DOPA modified. In each GAPDH simulation the monomer was used as a starting unit containing cofactor (NAD^+) and water molecules during the calculations and all movements were followed for 200 ps. To investigate the influence of GAPDH p-Tyr^{312} or DOPA-Tyr^{312} modification on enzymatic activity via NAD^+ binding affinity, the docking runs were performed with HADDOCK (37, 38). Docking was performed with default parameters using the Web server version of HADDOCK with a Refinement interface. To gain the Van der Waals, electrostatic, and desolvation energy for each enzyme, HADDOCK automatically performed the molecular dynamics before and after each docking trial by including water into the calculation. All structures were superimposed and differences were evaluated in UCSF Chimera.

Immunofluorescence and immunohistochemistry

Immunofluorescence of cells or tissues was performed with a Zeiss LSM 700 confocal microscope with a Plan-Apochromat 63x/1.40 Oil DIC M27 objective as described (8) using either TAMRA-labeled bacteria or bacteria-specific antibodies. In order to facilitate 3D data visualization, Fiji was used to create a maximum intensity projection from the Z-stacks. The first view from the 36 angles in projection is shown. Fixed rabbit tissue samples were processed, embedded in paraffin and cut into 5µm sections by microtome. Sections were deparaffinized

with xylene (10 min) and hydrated using an ethanol gradient (100% -6 min, 95% - 6 min, 70% - 3min) to distilled water (3min). Samples were stained with hematoxylin (7min) and eosin (3min). The stained slides were dehydrated (70% IMS-1min, 95% IMS-2min, 100% IMS-2min), cleared in xylene and mounted in DPX. Slides were analyzed using a Leica DFC300x camera and the IM50 imaging software. For detection of tissue protein carbonylation after infection the OxyIHC^{TM} Oxidative Stress Detection Kit (S7450 Millipore) was used.

Biofilm Assay

Biofilm was analyzed using SYTO9 (Life Sciences) as described by Oh and coworkers (39). Cultured bacteria were grown in microaerophilic conditions overnight. The bacterial culture was then adjusted to OD_{600}=0.1 and 1 ml of this solution was added to an optical grade plastic bottom µ-plate 24 well. Bacteria were incubated for an additional 72h in microaerophilic conditions. Bacteria were washed gently with autoclaved water to remove planktonic cells and fixed with 3% paraformaldehyde in PBS for 1h. Images were then analyzed for total intensity of SYTO9 fluorescence over the imaged volumes using Fiji. Briefly, after staining with SYTO9, 50 independent 13.2 µm stacks of 60 images at a 0.22 µm Z resolution were imaged for all conditions. The mean fluorescence of the different slices in the stacks was measured and a standard deviation was computed from the aggregated data per slice. The mean fluorescence with the corresponding standard deviations per slice was then plotted as a function of depth with the start of the stack set to zero.

Statistical Analysis

Data are expressed as mean ± SEM, n=3 or as indicated. Statistical differences between means were determined by a two-tailed unpaired Student's *t* test. In the figures, *** = P≤0.001; ** = P≤0.01 and * = P≤0.05.

Supplementary Figure Legends

Figure S1. NOX-p22^{phox} translocation in infected cells, biopsies and rabbit loops and protein expression controls

(a) Immunofluorescence images of p22^{phox} (green) plasma membrane localization (white arrows) in HCT-8 cells after 3h of infection with TAMRA-labeled bacteria (red). Nuclei stained with DAPI (blue). Scale bar 20 µm. (b) Immunofluorescence images of TAMRA-labelled *L. monocytogenes* (red) infection of biopsies; localization of p22^{phox} (green) is shown (3h). Nuclei stained with DAPI (blue). Scale bar 50µm. (c) Immunofluorescence images of p22^{phox} localization (green) in rabbit ileal loops after infection with *L. monocytogenes* (red) for 1.5h. Nuclei stained with DAPI (blue). Scale bar 20 µm. (d) H&E staining of rabbit ileal loop tissues injected with either PBS or *C. jejuni* for 3h. Scale bar 50 µm. (e) Localization of p22^{phox} NADPH oxidase subunit (green) in rabbit ileal loop tissues after treatment with PBS or *C. jejuni* for 3h. Nuclei stained with DAPI (blue). Scale bar 20 µm. (f) Coomassie blue staining of samples used for Fig. 1d (equal loading). (g) Anti-p-Tyr immunoblots of lysates derived from bacteria exposed to HCT-8 cells with and without catalase and loading control, see Fig. 1a. (h) Coomassie blue staining corresponding to Fig. 1e and anti-p-Tyr immunoblot of *S. typhimurium* exposed to Cos-NOX4 cells with loading control. (i) Coomassie blue staining corresponding to Fig. 1f. (j) Anti-*L. monocyt*. and anti-*C. jejuni* sera immunoblots of bacteria retrieved from rabbit loops as loading control for Fig. 1g.

Figure S2. Biochemical and functional analysis of intestinal bacteria

(a) Detection of Wzc by immunoblot using anti-*E.coli* Wzc antibody in *K. pneumoniae* lysates after treatment as in Fig. 1d. (b) Viability of *K. pneumoniae*, *L. monocytogenes* and *S. typhimurium* in the absence (black) or presence (red) of exogenous 0.7 mM H_2O_2. Viability was assessed at indicated time points. (c) Anti-p-Tyr immunoblot and Coomassie staining of lysates prepared from *K. pneumoniae* treated as indicated (65ºC o/n, 100ºC 10 min). (d) Anti-p-Tyr and anti-*C. jejuni* antisera immunoblots of lysates prepared from *C. jejuni* treated as indicated (65ºC o/n, 100ºC 10 min). (e) IEC adhesion and invasion of H_2O_2-preexposed *L. monocytogenes*. Error bars represent SEM and asterisks indicate significance (** $p \leq 0.01$ and * $p \leq 0.05$).

Figure S3. Characterization of the pulmonary pathogen *S. pneumoniae*

(a) H_2O_2 release by *ex vivo* cultured fetal rat lungs (rats R1, R2, R3) inoculated with *S. pneumoniae*. Rat lungs pretreated with DPI served as control. (b) Anti-p-Tyr immunoblot of *S. pneumoniae* collected from the lumen of infected rat lungs (3h). The starting bacterial culture and DPI-pretreated rat lungs served as controls. (c) Immunofluorescence image of rat lung alveolar macrophages 30 min after exposure to TAMRA-labeled *S. pneumoniae* (red). Localization of Nox2 (green) is depicted. Nuclei stained with DAPI (blue). Scale bar 5 μm. (d) H_2O_2 release by rat alveolar macrophages after 15 min of exposure to *S. pneumoniae* (+/- DPI pretreatment of cells). Error bars represent SEM and asterisks indicate significance (** $p \leq 0.01$). (e) H_2O_2 release measured in supernatant after 24h growth of *S. pneumoniae* in 21% O_2 or 5% O_2. Bacterial H_2O_2 in presence or absence of DPI is shown. (f) Anti-p-Tyr immunoblot of extracellular *S. pneumoniae* collected after exposure to alveolar macrophages (30 min). The starting bacterial culture and DPI served as controls. (g) Viability of *S. pneumoniae* at 5% O_2 in

the absence (black) or presence (red) of exogenous H_2O_2. Viability was assessed at indicated time points. (h) 3D measurement of *S. pneumoniae* biofilm in the presence (red) or absence (black) of H_2O_2. The mean fluorescent values for images in a 13.5 μm thick stack are shown. (i) Representative confocal image of *S. pneumoniae* biofilm (green) used for quantification in Fig. S3h. Scale bar 10 μm.

Figure S4. Production of recombinant Gne and Ugd, and identification of CetB as tyrosine kinase substrate

(a, e) Overexpression and purification of recombinant Gne and Ugd. Silver staining, anti-p-Tyr and anti-His immunoblotting of affinity purified (a) His-Gne or (e) His-Ugd expressed in *E.coli*. Both Gne and Ugd are tyrosine phosphorylated by *E. coli* BY-kinases in these conditions. (b) Anti-p-Tyr immunoblot of 2D gel electrophoresis of *C. jejuni* outer membrane proteins (OMPs). The arrow indicates the spot identified as CetB (CJJ81176_1204) by MS-MS. (c) Coomassie stained gel and anti-His immunoblot of His-tagged CetB, expressed and affinity purified from *E. coli*. FT denotes flow through. (d) Anti-p-Tyr immunoblot depicting CetB dephosphorylation by recombinant *C. jejuni* cytochrome P450 in the presence of H_2O_2. Dithionite served as inhibitor of cytochrome P450 activity. Anti-His blot served as loading control.

Figure S5. MS/MS analysis of oxidized Gne and Ugd

(a) MS/MS data representative of the *C. jejuni* Gne (A1W0B7_CAMJJ) peptide (aa 117-150). The full sequence of Gne with the peptide containing the active site is also shown in brackets. The peaks corresponding to the DOPA formation are indicated with arrows. (b) MS/MS data representative of the *E. coli* Ugd peptide (aa 68-88). The full sequence of Ugd with the peptide

containing the phosphotyrosines that modulate Ugd function is in brackets. The peak corresponding to DOPA formation is indicated with an arrow.

Figure S6. MS/MS data of the phosphopeptide and dityrosine formation on Gne or Ugd in the presence of free tyrosine

(a-d) MS/MS data from peptide experiments representative of chromatograms in Figure 4c, d. Tyrosyl residue indicated with an arrow. (a) Starting peptide with 100% phosphorylation on tyrosine. (b) DOPA formation on the p-Tyr position in the presence of CjP450/HRP and 1mM H_2O_2. Expected net mass shift of -63 Da. (c) Dityrosine formation in the presence of CjP450/HRP, 1mM H_2O_2 and free tyrosine in excess. Expected net mass shift +100 Da. (d) 18O addition to tyrosine in the presence of CjP450/HRP and 1mM ^{18}O H_2O_2. Expected net mass shift of -61 Da from the starting material or +2 Da from ^{16}O oxidation. (e, f) Representative MS-MS spectra showing mass fingerprint sequencing from protein experiments in Figures 4f, g. The position for dityrosine addition is indicated (arrows) on (e) Gne (aa 117-150) and (f) Ugd (aa 68-88) respectively.

Figure S7. Putative chemical mechanisms underlying the loss of tyrosine phosphorylation and emergence of DOPA modification in the H_2O_2-mediated reaction of cytochrome P450 with Gne.

Figure S8. Gne and Ugd 3D models highlighting tyrosyl residues with dityrosine modifications detected in this study

Cartoon showing identified Gne (a) and Ugd (b) tyrosyl residues found to undergo a dityrosine modification in red. Multiple dityrosine formations are possible, although not all sites lead to

DOPA modification. Numbers in parenthesis correspond to the solvent accessibility surface area for each dityrosine residue.

Table S1. Bacterial peptides with corresponding DOPA and p-Tyr modifications

DOPA-modified tryptic peptides identified in this study (H_2O_2, NOX4) or in literature (DOPA, (27)) that correlate to identified p-Tyr sites in *K. pneumoniae* (9) and *E. coli* (12).

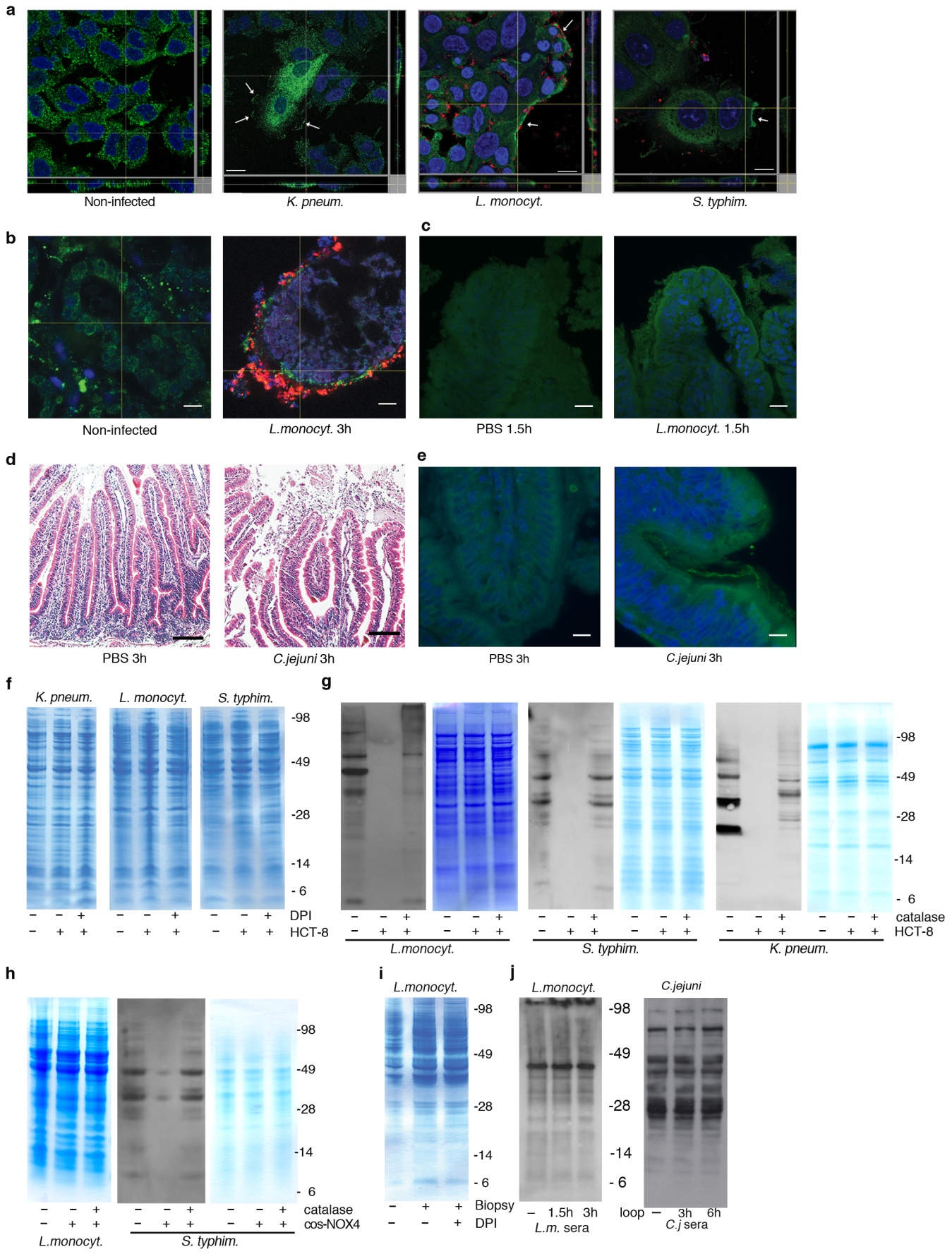
a
Non-infected
K. pneum.
L. monocyt.
S. typhim.
b
Non-infected
L.monocyt. 3h
c
PBS 1.5h
L.monocyt. 1.5h
d
PBS 3h
C.jejuni 3h
e
PBS 3h
C.jejuni 3h
f
K. pneum.
L. monocyt.
S. typhim.
-98
-49
-28
-14
- 6
DPI
HCT-8
g
L.monocyt.
S. typhim.
K. pneum.
catalase
HCT-8
h
catalase
cos-NOX4
L.monocyt.
S. typhim.
i
L.monocyt.
Biopsy
DPI
j
L.monocyt.
C.jejuni
1.5h 3h
L.m. sera
loop 3h 6h
C.j sera